Electrochimica Acta 424 (2022) 140642

Contents lists available at ScienceDirect

Electrochimica Acta

journal homepage: www.journals.elsevier.com/electrochimica-acta

Glyoxylic acetals as electrolytes for Si/Graphite anodes in lithium-ion batteries

Lydia Gehrlein [a], Christian Leibing [b,c], Kristina Pfeifer [a], Fabian Jeschull [a], Andrea Balducci [b,c], Julia Maibach [a,*]

[a] Karlsruhe Institute of Technology (KIT), Institute for Applied Materials - Energy Storage Systems (IAM-ESS), Hermann-von-Helmholtz-Platz 1, Eggenstein-Leopoldshafen 76344, Germany
[b] Institute for Technical Chemistry and Environmental Chemistry, Friedrich Schiller University Jena, Philosophenweg 7a, Jena 07743, Germany
[c] Center for Energy and Environmental Chemistry Jena (CEEC Jena), Friedrich Schiller University Jena, Philosophenweg 7a, Jena 07743, Germany

A B S T R A C T

Using silicon-containing anodes in lithium-ion batteries is mainly impeded by undesired side reactions at the electrode/electrolyte interface leading to the gradual loss of active lithium. Therefore, electrolyte formulations are needed, which form a solid electrolyte interphase (SEI) that can accommodate to the volume changes of the silicon particles. In this work, we analyze the influence of two glyoxylic acetals on the cycling stability of silicon-containing graphite anodes, namely TMG (1 M LiTFSI in 1,1,2,2-tetramethoxyethane) and TEG (1 M LiTFSI in 1,1,2,2-tetraethoxyethane). The choice of these two electrolyte formulations was motivated by their positive impact on the thermal stability of LIBs. We investigate solid electrolyte decomposition products employing x-ray photoelectron spectroscopy (XPS). The cycling stability of Si/Gr anodes in each electrolyte is correlated to changes in SEI thickness, composition, and morphology upon formation and aging. This evaluation is completed by comparing the performance of TMG and TEG to two carbonate-based reference electrolytes (1 M LiTFSI in 1:1 ethylene carbonate: dimethyl carbonate and 1 M $LiPF_6$ in the same solvent mixture). Cells cycled in TMG display inferior electrochemical performance to the two reference electrolytes. By contrast, cells cycled in TEG exhibit the best capacity retention with overall higher capacities. We can correlate this to better film-forming properties of the TEG solvent as it forms a smoother and more interconnected SEI, which can better adapt to the volume changes of the silicon. Therefore, TEG appears to be a promising electrolyte solvent for silicon-containing anodes.

1. Introduction

To fulfill increasing market demands, Li-ion batteries are required to deliver higher energy and power densities and be safer during operation compared to state-of-the-art batteries. Higher energy densities can be obtained by increasing the specific charge of the anode material. This is achieved by blending graphite with a low amount of a material with high theoretical specific capacity such as silicon ($Q_{th} = 3579$ mAh g^{-1}) [1–8]. However, silicon exhibits high volume changes during (de)lithiation processes amounting up to 280% [1,9,10]. As the silicon volume is continuously changing upon cycling, the electrode material is gradually pulverized and parts of the active material become isolated [1, 9–12]. Furthermore, the large volume expansions and contractions expose the SEI to high mechanical strain [11,13–16]. The SEI is a result of electrolyte instability in the applied voltage range (~below 1 V vs. Li/Li^+) and consists of insoluble electrolyte decomposition products [17]. While this layer allows lithium-ion transport, it is electrically insulating and thereby decreases further electrolyte decomposition. Thus, the electrode surface is passivated, and long-term cycling becomes possible. A well-functioning SEI is therefore essential for the long-term stability of a battery. This is especially the case with Si/Gr anodes, where the SEI oftentimes cannot accommodate the electrode volume changes. Consequently, cracks are formed, which causes a re-exposure of Si-/Gr electrode material to the electrolyte, leading to new SEI formation. Every electrolyte decomposition reduces the lithium reservoir and ultimately leads to the failure of the cell. Hence, electrolyte formulations are needed which can accommodate to these volume changes.

State-of-the-art electrolytes consist of a lithium salt (e.g., lithium-hexafluorophosphate - $LiPF_6$) dissolved in a mixture of a cyclic carbonate of high dielectric constant (e.g., ethylene carbonate - EC) with a linear carbonate of low viscosity (e.g., dimethyl carbonate - DMC). These solvent combinations result in low viscosities and high ionic conductivities [18,19]. Drawbacks are mainly safety issues and thermal instabilities of both, electrolyte salt and solvent [20,21]. When cycled with carbonate-based electrolytes such as LP30 (1 M $LiPF_6$ in 1:1 EC: DMC), Si/Gr anodes show poor capacity retention. Besides silicon and

* Corresponding author.
E-mail address: julia.maibach@kit.edu (J. Maibach).

https://doi.org/10.1016/j.electacta.2022.140642
Received 17 February 2022; Received in revised form 6 May 2022; Accepted 26 May 2022
Available online 27 May 2022

electrode degradation effects, the SEI formed by the LP30 electrolyte is one reason for the insufficient capacity retention, which is linked presumably to unfavourable SEI properties, such as insufficient flexibility upon volume expansion. To improve the cycling stability of Si/Gr electrodes, sacrificial electrolyte additives such as fluoroethylene carbonate (FEC) are used [11,16,22–24]. Upon decomposition, FEC is suggested to form elastomeric poly(VC)-type species thereby increasing the SEI flexibility upon electrode volume changes [25]. However, as FEC is consumed with each cycle, the capacity stabilizing effect disappears the moment the additive is exhausted [13,26].

Investigations of alternatives to carbonate-containing electrolytes such as LP30 focus on overcoming safety issues and thermal instability, as well as better SEI forming properties. Several alternative electrolytes have been studied in the last years. Among them, those based on glyoxal solvents such as 1,1,2,2-tetramethoxyethane (TMG) and 1,1,2,2-tetraethoxyethane (TEG) appear interesting because their use indicates a positive impact on the thermal stability of LIBs [27–30]. Used with graphite-based LIBs, electrolytes based on TEG or TMG and lithium bis (trifluoromethansulfonyl)imide (LiTFSI) as electrolyte salt showed good cyclability at room temperature and 60°C [27,30,31]. However, some issues remain with this solvent class as TMG and TEG for example exhibit lower ionic conductivities and higher viscosities compared to carbonates. These disadvantages can be overcome by mixing glyoxylic acetals with other solvents such as propylene carbonate [28,29]. Also, the SEI formed by glyoxal-based electrolytes has yet to be investigated.

Therefore, we focus in this work on the SEI properties derived from glyoxal-based electrolytes. We report for the first time about the effect of glyoxal-based electrolytes 1 M LiTFSI in TMG and 1 M LiTFSI in TEG (Fig. 1) on the cycling stability of Si/Gr anodes. To simplify the system, we omit using organic carbonates as ionic conductivity boosters and focus only on analyzing pure glyoxal-based electrolytes. For comparison, two reference electrolytes namely LP30 (1 M $LiPF_6$ in 1:1 EC: DMC) and L-E/D (1 M LiTFSI in 1:1 EC: DMC) have also been investigated. To study the electrochemical behavior of these electrolytes, we use a half-cell setup containing Si/Gr working electrodes and lithium metal counter electrodes. X-ray photoelectron spectroscopy (XPS) is used to evaluate changes in SEI thickness and composition upon formation and aging. In addition, the electrode morphology is analyzed via scanning electron microscopy (SEM). Finally, we correlate the different SEI characteristics to the electrochemical performance.

2. Experimental

2.1. Electrolyte preparation

Battery-grade LP30 (i.e., 1 M $LiPF_6$ in 1:1 ethylene carbonate: dimethyl carbonate) electrolyte (Merck) was used as received (water content <10 ppm as measured by Karl-Fischer titration). The solvents DMC and EC as well as the LiTFSI salt were purchased from Merck and dried over a molecular sieve before usage (water content <15 ppm as measured by Karl-Fischer titration). The solvents TMG and TEG were obtained from Weylchem and dried with an over-pressure Schlenk filtration through vacuum-pre-dried aluminum oxide. The water content for both solvents was reduced to under 20 ppm, as measured by Karl-Fischer titration.

2.2. Electrode preparation

Electrodes were prepared using a slurry of 81 wt% graphite (SFG6L, TIMCAL), 9 wt% silicon nanopowder (Nanostructured & Amorphous Materials Inc., 50-100 nm, purity > 99%), 5 wt% carbon nanofibers (Showa Denko), and 5 wt% lithium-polyacrylic acid binder solution. The binder solution was obtained by diluting a ready-made 45 wt% polyacrylic acid in water solution (Sigma Aldrich) and subsequently adding lithium-hydroxide (LiOH, Sigma Aldrich) until a pH of 5 was reached. In the following, the lithium polyacrylate binder is referred to as LiPAA. The slurries were prepared in a two-step process. The premixing was done with a planetary mixer (Thinky ARV-310P). Firstly, silicon nanopowder (9 wt%) was mixed with carbon nanofibers (5 wt%) and graphite (81 wt%) in water: ethanol mixture of 1:1.2. Subsequently, the mixture was dried and gradually transferred into a glass vial containing the LiPAA solution. To break particle agglomeration, mixing was performed via ultrasonic dispersion with an ultrasonic homogenizer (Kinematica, Polytron PT 2500). The obtained slurry was coated on a copper foil with a doctor blade (wet thickness was set to 150 μm) and later dried at room temperature overnight. Individual electrodes were cut into discs with 12 mm in diameter and dried under vacuum at 120°C for 12 h. The resulting electrodes had a silicon-graphite mass loading of around 2.5 mg/cm^2.

2.3. Half-cell assembly and cycling

The electrodes were assembled in an Ar-filled glovebox in a CR2025-type coin cell half-cell setup. All cells consisted of the Si/Gr working electrode, a microporous polypropylene separator (Celgard 2325), a glass fiber separator (VWR), and Li foil (thickness: 0.25mm, purity: 99.9%, PI-KEM) as counter electrode. The Celgard 2325 separator was applied directly on the electrode surface to protect it from possible glass fiber contaminations. 150 μL of the respective electrolyte solution was used (see Table 1). Galvanostatic cycling with potential limitation (GCPL) was performed with a multichannel potentiostat (VMP3 & BCS, Bio-Logic) at 25°C in a climate chamber (Binder). After one formation cycle at C/20 (1C = 623 mAh g^{-1}), all cells were cycled at a rate of C/10 between 1.5 V - 0.01 V. After every lithiation step, a constant-current constant-voltage (CCCV) was applied at C/5 for 30 minutes.

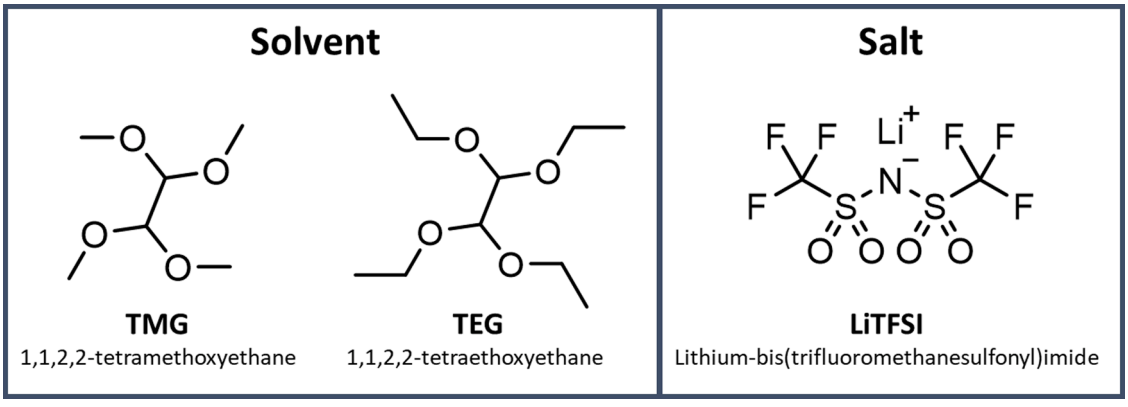

Fig. 1. Molecular structures of 1,1,2,2-tetramethoxyethane (TMG), 1,1,2,2-tetraethoxyethane (TEG), and lithium bis(trifluoromethansulfonyl)imide (LiTFSI).

Table 1
Overview of the used electrolyte compositions.

Electrolyte	Composition
LP30	1 M $LiPF_6$ in 1:1 ethylene carbonate:dimethyl carbonate (Merck, battery grade)
L-E/D	1 M LiTFSI (Merck) in 1:1 ethylene carbonate (Merck): dimethyl carbonate (Merck)
TEG	1 M LiTFSI (Merck) in 1,1,2,2-tetraethoxyethane (Weylchem)
TMG	1 M LiTFSI (Merck) in 1,1,2,2-tetramethoxyethane (Weylchem)

2.4. Post-mortem analysis (XPS & SEM)

All samples were washed by a 1-minute submersion in the following solvents: For LP30 and L-ED, dimethyl carbonate (DMC) was used. For the glyoxal electrolytes, the respective solvent (i.e.,1,1,2,2-tetraethoxyethane or 1,1,2,2-tetramethoxyethane) was applied. After washing, all electrodes were dried and mounted on a sample holder using conductive copper tape. The sample preparation was carried out in an argon-filled glove box (H_2O & O_2 <1ppm). Transfer to the photoelectron spectrometer or the SEM was done via a transfer module under inert gas conditions. To ensure SEI stability in lithiated and delithiated states, the lithiation and delithiation endpoint potentials were held for 1 hour after the electrochemical cycling.

X-Ray photoelectron spectroscopy (XPS). XPS measurements were carried out with a K-alpha spectrometer from Thermo-Fisher Scientific applying a micro-focused, monochromated Al-K_α X-Ray source with 400 µm spot size. A pass energy of 50 eV was used. Data acquisition and handling were done via the Thermo Avantage software by K.L. Parry *et al.* [32]. Spectra were fitted with one or more Voigt profiles and Scofield sensitivity factors were applied for quantification. All spectra are referenced in binding energy to the hydrocarbon C 1s peak at 285 eV. For clarity of presentation, all spectra are normalized in intensity to the maximum intensity.

Scanning electron microscopy (SEM). Scanning electron microscopy (SEM) measurements were conducted using a thermal field emission scanning electron microscope (FESEM, Carl Zeiss SMT AG) equipped with energy-dispersive spectroscopy (EDS, Quantax 400 SDD, Bruker) at an acceleration voltage of 7 kV.

3. Results & discussion

3.1. Electrochemistry

Galvanostatic cycling of Si/Gr half-cells cycled in the respective electrolytes TMG (blue), TEG (black), L-E/D (green), and LP30 (pink) are shown in Fig. 2a. Corresponding columbic efficiencies are displayed in Fig. 2b. As shown during the 1st cycle, the electrodes exhibit higher specific lithiation capacities than the theoretical values in all 4 investigated electrolytes. This is due to extensive SEI formation during this first cycle. The cell cycled in the L-E/D electrolyte displays the highest lithiation capacity with 964 mAh g^{-1}. Also, the largest irreversibility appears for L-E/D as can be seen in the coulombic efficiency of only 71%. Cells cycled in TMG, TEG, and LP30 display lower initial lithiation capacities of around 780 mAh g^{-1} and higher columbic efficiencies of around 80%.

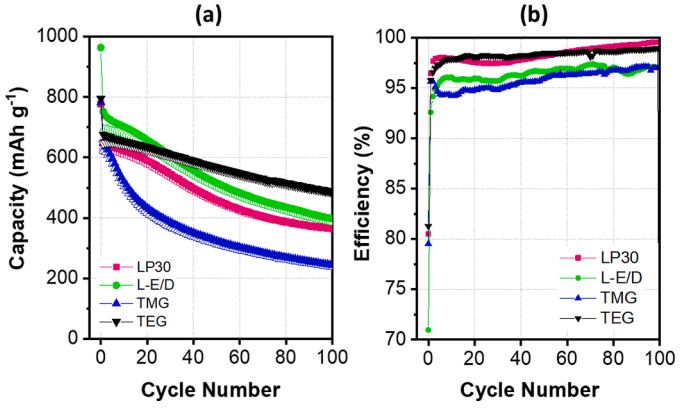

Fig. 2. (a) Cycling stabilities and (b) coulombic efficiencies of Si/Gr electrodes cycled in TMG (blue), TEG (black), L-E/D (green), and LP30 (pink) electrolytes.

Upon cycling, the cell with the TMG electrolyte displays the fastest capacity drop out of all electrolytes. Already after 10 cycles, a decline of around 100 mAh g^{-1} can be observed. This decrease is reflected by a decline in coulombic efficiencies of 1.5%, indicating a possible loss of active material and solid electrolyte interphase evolution. After 100 cycles, only 38% of capacity can be retained from the 647 mAh g^{-1} observed in the 2nd cycle. In comparison, cells cycled in TEG show the smallest capacity decrease out of all electrolytes. After 100 cycles, 488 mAh g^{-1} are retained (i.e., 72%). Coulombic efficiencies remain at around 98.9% throughout the cycling experiment. When using the two reference electrolytes LP30 and L-E/D better performances are achieved compared to the TMG case. However, the capacity retention is much worse than in presence of TEG. A significant capacity drop can be seen after 15 cycles for both carbonate-based electrolytes, leading to a retention of 53% and 56% after 100 cycles, respectively.

Fig. 3 compares the evolution of the differential capacity (dQ/dE) of the Si/Gr electrodes for selected cycles over the first 100 cycles. Regardless of the used electrolyte, the Si/Gr electrodes generally display the same electrochemical processes, but with different rates of intensity decay for the characteristic intercalation/alloying peaks. In all systems, the first cycle shows the most intense dQ/dE signals during both lithiation and delithiation. The following graphite lithiation intercalation reactions are observed: 0.2 V (stage IV), 0.13 V (stage III, LiC_{30}), 0.1 V (stage II, LiC_{12}), and 0.07 V (stage I, LiC_6) [33,34]. Lithiation of crystalline silicon occurs via a two-phase mechanism in which crystalline silicon is transformed to lithiated amorphous silicon (Li_xSi) [35–38] The alloying reactions extend over the whole lithiation profile and are difficult to distinguish from the graphite intercalation signals. At the end of the first lithiation, the amorphous Li_xSi phase reacts to crystalline $Li_{15}Si_4$, corresponding to the minima at 0.04 V in the dQ/dE plot [39–41]. Upon delithiation, the crystalline $Li_{15}Si_4$ transforms back to amorphous silicon in which state it remains during the whole delithiation. In the dQ/dE profile of the 10th cycle, a new signal can be observed at 0.3 V for all electrolytes corresponding to the lithiation of the amorphous silicon.

Cells cycled in the TMG electrolyte show the most pronounced intensity decrease upon cycling. Already after 10 cycles, a large amount of graphite and silicon activity is lost, reflecting the dramatic capacity drop observed in Fig. 2. Both reference electrolytes L-E/D and LP30 show higher electrochemical activity than TMG, which results in the higher capacity retentions observed in Fig. 2. Especially graphite intercalation reactions are better retained upon cycling. However, both silicon and graphite show losses in activity, mirroring the capacity drop in Fig. 2. By contrast, when using TEG, only small losses in silicon activity are observed as can be seen in the signal at 0.3 V and 0.04 V from the 10th to the 100th cycle. Moreover, the electrochemical activity of graphite is completely retained throughout the GCPL experiment. This better retention in the activity of both silicon and graphite explains the improved electrochemical performance displayed in Fig. 2.

At this stage, neither electrolyte viscosity nor ionic conductivity appear to play a role. For TMG and TEG, both parameters are very similar, however, their electrochemical performances are very different. Compared to L-E/D and LP30, TEG has much higher viscosities and lower ionic conductivities. However, much higher capacity retention is achieved during cycling with TEG. Different film-forming abilities might be one reason for the observed differences in electrochemical activity, as will be discussed in the following part of this manuscript.

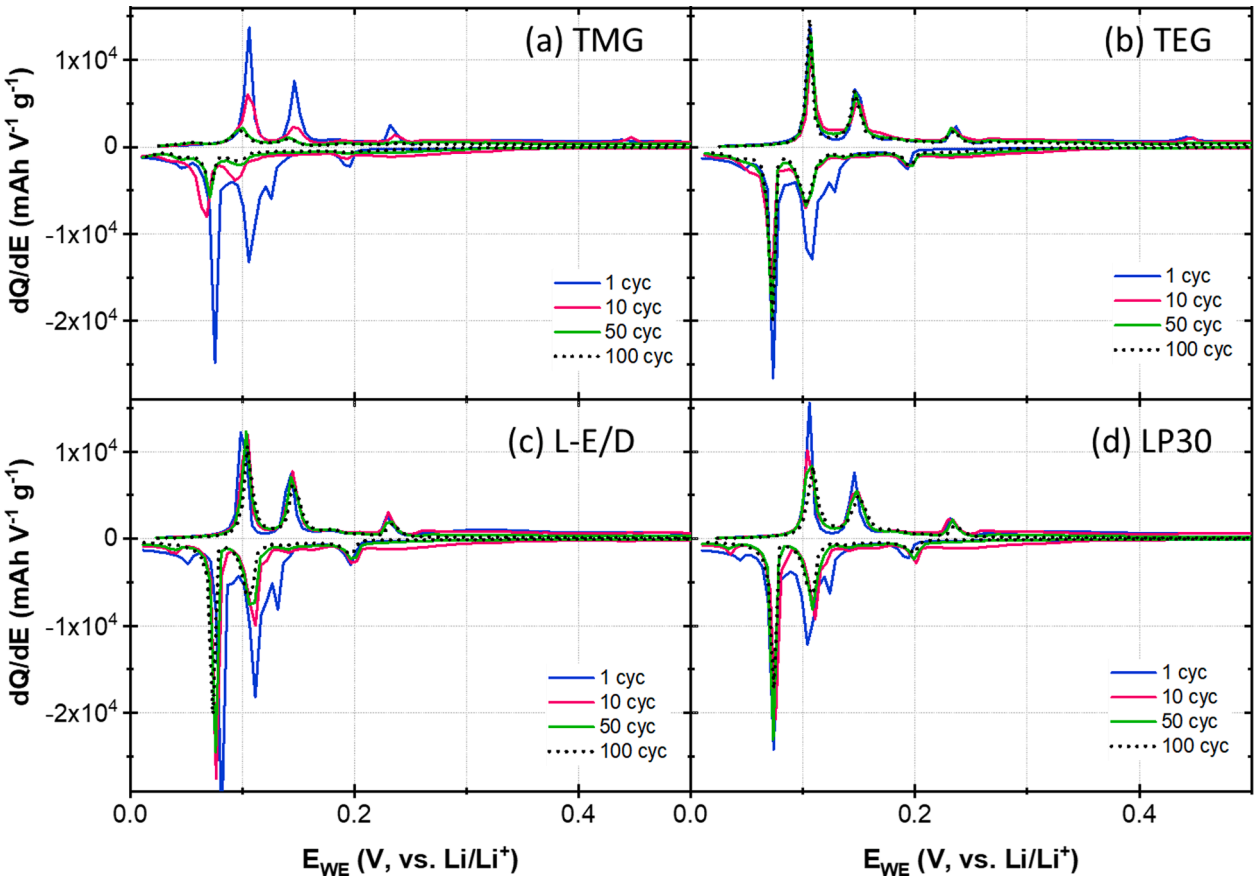

Fig. 3. Differential capacities of dQ/dE plot of Si/Gr electrodes cycled in TMG (a), TEG (b), L-E/D (c), and LP30 (d) electrolytes.

3.2. SEI analysis

Glyoxalic acetal decomposition products. To analyze the properties of TMG and TEG film formation, solid decomposition products of these electrolytes are characterized by XPS and used as the basis for all XPS analyses to follow. Fig. 4 shows the C1s spectra of Si/Gr electrodes in their pristine state, as well as after the first lithiation with TMG and TEG electrolytes. The spectrum of the pristine electrode demonstrates peaks corresponding to the electrode material, namely graphite (284.6 eV) and -CO_2Li-groups of the LiPAA binder (288.4 eV). Hydrocarbons associated with both adventitious carbon and LiPAA emerge at 285 eV. After lithiation in the respective glyoxal electrolytes, four peaks are observed: -CH (285 eV), -C-O (286.5 eV), -CO_2 (i.e., carboxylic -C(=O)O environment at 289 eV), and -CO_3 (i.e., carbonate -O(C=O)O environment at 290.4 eV). While the formation of carbonates upon reduction of glyoxales might seem unusual, electrochemical reactions of e.g., CO_2 and lithium are possible. Carbonate species are known to form by reaction of CO_2 with lithium [42]. Furthermore, the binding energy of 290.4 eV is typical for carbonate environments. Another indicator is a relation close to 1 between the atomic percentages of -C=O species detected in the C1s and the O1s spectrum (see Table S1 for more information).

SEI thickness. The SEI thickness was determined by an approximation in which the graphite C1s intensity of a pristine electrode is divided by the graphite C1s intensity after cycling, see Fig S1. Thereby, an attenuation value is obtained which indicates how much the intensity of the graphite signal is weakened by the SEI layer. The thus obtained SEI thickness approximations or attenuation values at different potentials during the first lithiation (i.e., at 2.5 V, 1.3 V, 0.9 V, 0.5 V, and 0.01 V) as well as after the 1st, the 10th, and 100th cycle (all in the delithiated state at 1.5 V) are displayed in Fig. 5. The formation potentials are motivated by specific minima in the differential capacity plots of Fig. S2.

During the first lithiation at 2.5 V and 1.3 V, less graphite is detected for cells containing LiTFSI-salt i.e., TMG, TEG, and L-E/D. In presence of $LiPF_6$ (i.e., LP30 electrolyte) the detected graphite intensity is higher. However, only small changes are observed in the attenuation between these two potentials, which indicates similar surface layer thicknesses. At 0.9 V, the observed attenuation values decrease in all four cases from around 0.9 - 0.6 to 0.5 - 0.3 indicating an increase in layer thickness. This increase coincides with the electrochemically observed onset of electrolyte decomposition (i.e., 1.5-1.0 V vs. Li/Li$^+$) seen in Fig. S3. The attenuation values continue to drop at 0.5 V to below 0.2 for TMG and TEG. In comparison, both carbonate-containing electrolytes, L-E/D and LP30 display higher attenuation values and therefore a thinner SEI layer. At 0.01 V, no graphite is observed for any electrolyte. Thus, the SEI is thicker than 5-10 nm, which corresponds to the probing depth of the x-ray photoelectron spectrometer. After the 1st delithiation, graphite reappears in the case of TMG, TEG, L-E/D, and LP30. Such SEI layer thickness increase during lithiation and decrease during delithiation is already known in literature. Especially in presence of silicon, the SEI layer is known for such a “breathing behavior” [43–45]. It can be explained by a mechanical instability of the SEI during the silicon volume decrease from the lithiated to the delithiated state. Thereby, graphite is re-exposed and can be detected via XPS due to emerging cracks in the SEI or parts of it detaching or dissolving into the electrolyte. After 10 cycles, no graphite is observed for TMG and TEG while it is still being detected for L-E/D and LP30. There can be two reasons for this observation: 1) glyoxal-based electrolytes decompose to a stronger degree, which would lead to a faster SEI coverage of the electrode, or 2) glyoxal-based electrolyte accommodate to the electrode volume changes to a higher degree. After 100 cycles, graphite disappears in all cases suggesting a considerable SEI layer is build-up during longer cycling.

Overall, the electrolyte solvent seems to play a more important role

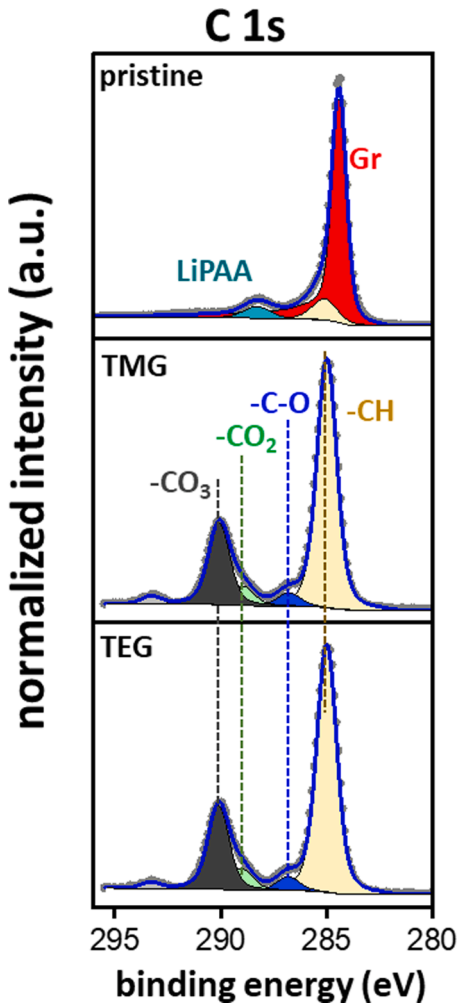

Fig. 4. C1s photoelectron spectra of pristine and cycled Si/Gr electrodes. The cycling was done in TMG-LiTFSI and TEG-LiTFSI electrolyte, respectively.

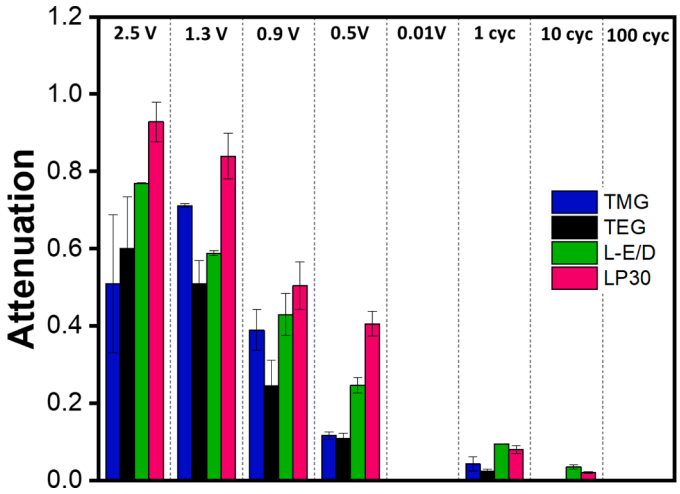

Fig. 5. Thickness approximation of the SEI formed by TMG, TEG, L-E/D, and LP30 electrolyte decomposition. The error bars indicate the standard deviation between two measurements on one electrode.

in SEI thickness than the electrolyte salt. We detect higher similarities between the same group of electrolyte solvents than we do for the same electrolyte salt. The SEI thicknesses of electrolytes containing carbonate solvents (i.e., LP30 and L-E/D) are more comparable to each other, as are the thicknesses between electrolytes containing glyoxal solvents (i.e., TMG and TEG). In contrast, the thicknesses of LiTFSI-containing TMG, TEG, and L-E/D are much less comparable. Also, TMG and TEG show similar absolute values and trends in attenuation, which would suggest similar SEI thicknesses during the first ten cycles. Possible changes in SEI thickness upon longer cycling, especially when the achievable capacities and thus the amount of active material being (de) lithiated differ significantly from each other, cannot be detected because of the limited probing depth of XPS (i.e., 5-10 nm).

Evolution of SEI composition during formation. To understand the SEI formation in the investigated electrolytes, electrodes were cycled up to 2.5 V, 1.3 V, 0.9 V, 0.05 V, and 0.01 V in the first cycle, and subsequently analyzed via XPS. C 1s spectra are displayed in Fig. 6 and the atomic percentages derived from these data are summarized in Fig. 7. The corresponding F1s spectra and the atomic percentage evaluation are presented in Figs. 8 and 9, respectively. N1s, O1s, P2p, and S2p spectra can be found in the supporting information, Figs. S4-6. An overview of all detected species can be found in Tables S2-5. Assignment of different surface species follows previous reports in literature [46,47].

Solvent decomposition. The C1s spectra of Fig. 6 show electrodes cycled in TMG and TEG electrolyte to display very similar C 1s spectra at 2.5 V and 1.3 V. Six peaks are observed in each spectrum: graphite (284.8 eV) with its corresponding π→π* shake-up (290.8 eV), hydrocarbons (285 eV) caused by LiPAA, adventitious carbon and in case of TEG also by -CH groups, H_3C-O- or -H_2C-O-groups (286.5 eV) resulting from the TMG and TEG solvent respectively, -CO_2 groups (carboxylic environment at 289 eV) of the LiPAA binder, and -CF_3 groups (293.4 eV) caused by the LiTFSI salt. The -O-C-O-groups of both the TEG and TMG molecules cannot be seen in the C1s spectra due to the low amount of TEG and TMG present on the surface. At these voltages, the measured electrolyte components (i.e., TEG or TMG solvent and LiTFSI salt) most probably correspond to solvent and electrolyte salt residues and not to electrolyte decomposition products. Electrolyte solvent residues might derive from the electrode washing process. TEG and TMG are used as washing solvents after cycling. As they have high vapor pressures, the respective solvent might not completely evaporate, and a small residue remains on the surface.

At 0.9 V, a distinct difference in surface composition is observed. A new peak emerges corresponding to -CO_3 (290.4 eV). Hydrocarbons, -C-O, and -CO_2-containing compounds are increasing in intensity, while the graphite intensity is decreasing. These observations indicate the decomposition of the glyoxal solvents. When lowering the potential further down to 0.5 V and 0.01 V, the SEI components continue to increase, while graphite decreases in intensity. In the fully lithiated state, the SEI is so thick that no more graphite is detected. Here, the C1s spectra are dominated by hydrocarbons (~22 at.%) and -CO_3 containing compounds (~7 at.%), see Fig. 7. Overall, TMG and TEG display very similar C1s spectra as well as atomic percentages of the different carbon surface species.

C1s spectra of electrodes cycled in the two reference electrolytes LP30 and LiTFSI-EC/DMC show four peaks at 2.5 V, corresponding to graphite (284.4 eV) with the corresponding π→π* shake-up (290.8 eV), adventitious carbon and -CC/CH groups at 285 eV, and -CO_2-groups of the LiPAA binder (288 eV). L-E/D shows an additional peak corresponding to -CF_3 groups of the LiTFSI salt (293.3 eV). Substantial changes in the C1s spectra can be observed for both reference electrolytes when the cell potential is lowered to 0.9 V. At this stage, a decrease in graphite intensity is detected, while the intensities for hydrocarbons and -CO_2-groups are increasing. The -CO_2-groups now correspond to EC/DMC decomposition products, rather than to the LiPAA binder. Furthermore, two new peaks are observed corresponding to -C-O (286.5 eV) and -CO_3-groups (290.3 eV) of EC/DMC decomposition products. The -C-O-component at 286.5 eV could also be attributed to carbon neighboring a carbonate group (i.e. -**C**-CO_3-), as is the case for alkyl-carbonates [48]. Alkyl-carbonates such as lithium ethylene

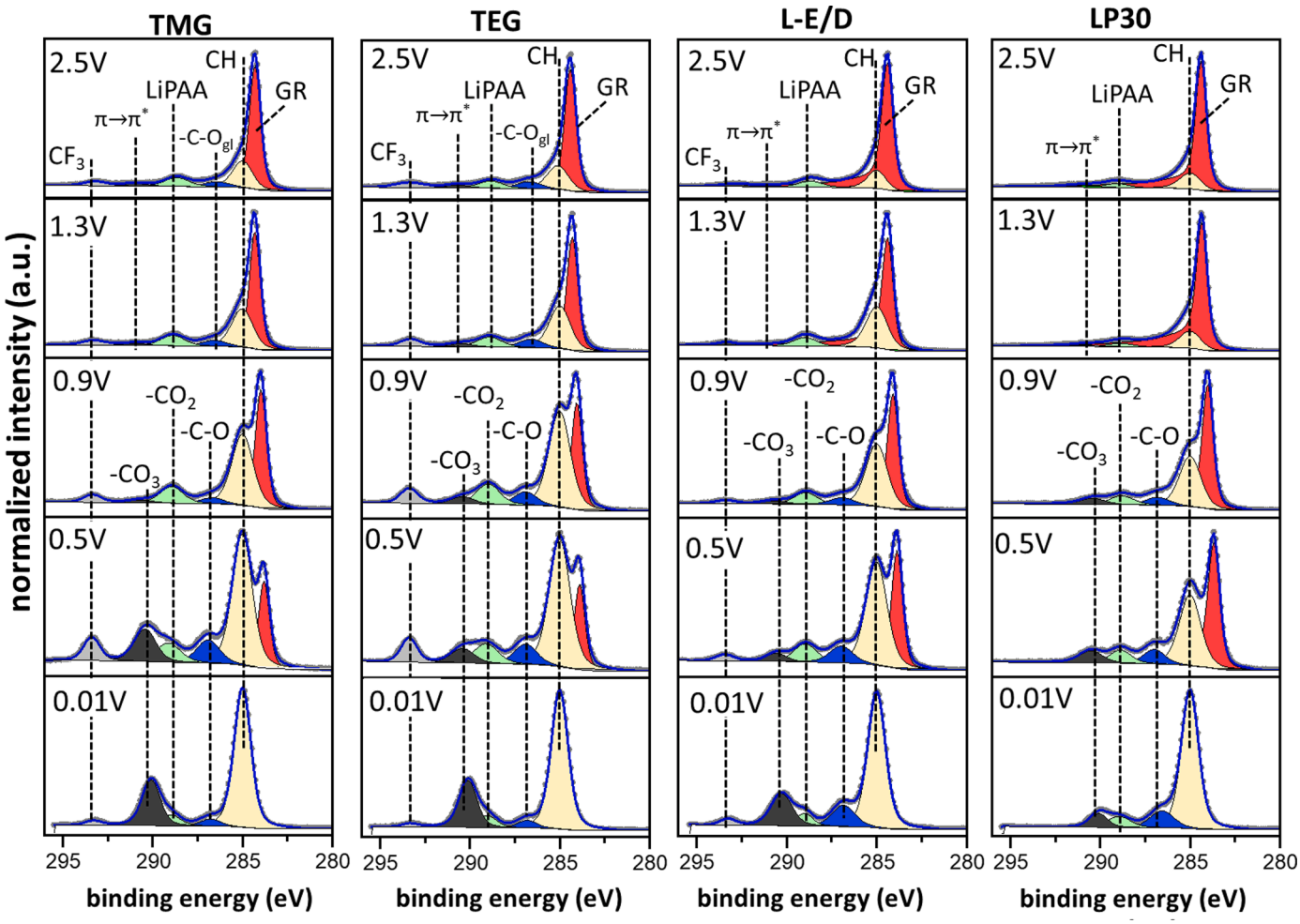

Fig. 6. C 1s photoelectron spectra of electrodes cycled in TMG, TEG, L-E/D, and LP30 electrolyte at 2.5 V, 1.3 V, 0. 9 V, 0.5 V, and 0.01 V during 1st lithiation.

dicarbonate are typical degradation products of carbonate-containing electrolytes [42,49]. At 0.5 V and 0.01 V, all SEI components continue to increase in intensity, indicating ongoing electrolyte solvent decomposition. The amount of detected graphite further decreases and disappears completely in the fully lithiated state. A previous XPS study on graphite electrodes showed comparable SEI evolution over cycling for both L-E/D and LP30 electrolytes, respectively [50]

Both glyoxal- and carbonate-based solvents show initial SEI formation between 1.5 V and 0.9 V, which is also supported by the dQ/dE plots in Fig. S2. In the fully lithiated state, they display similar amounts of hydrocarbons, while -C-O compounds are more abundant for L-E/D and LP30. The -CO_2 species are similar for TMG, TEG, and LP30, but more abundant for L-E/D. Carbonate-containing compounds are more abundant for the LiTFSI containing electrolytes, i.e., TMG, TEG, and L-E/D but less present for the $LiPF_6$ containing LP30.

Salt components and decomposition. LiTFSI is suggested to be reduced via the intermediate product $LiSO_2CF_3$ to a combination of LiF, Li_2S, $Li_2S_2O_4$, Li_2SO_3, Li_2SO, and Li_3N [51–53]. It was further proposed for LiTFSI to form $C_2F_xLi_y$-like compounds [53]. In Fig. 8, F1s spectra of cells cycled in TMG and TEG display two peaks corresponding to -CF_3 (689.1 eV) and LiF (685.1 eV). At higher potentials such as 2.5 V and 1.3 V, the -CF_3 peaks most probably correspond to residual LiTFSI electrolyte salt. At lower voltages, the LiTFSI-CF_3 peak overlaps with possible -CF_3 containing decomposition products. However, we cannot differentiate between -CF_3 groups which correspond to either salt or salt decomposition products. As can be seen in Tables S2-4, the ratio of -C**F**$_3$, -**N**-SO_2, and -**S**O_2 match the ratios observed in LiTFSI. This increases the possibility for -CF_3 to belong to the LiTFSI salt. Because the intensity is normalized to a scale of 0 to 1, changes in the detected -CF_3 species cannot be readily analyzed from the shown graphs. Therefore, the absolute atomic percentages displayed in Fig. 9 are examined. At higher potentials (i.e., from 2.5 V to 0.5 V), both LiTFSI-containing TMG and TEG electrolytes demonstrate only small changes in atomic percentages of the -CF_3 species. In the fully lithiated state at 0.01 V, both display a decline in the detected -CF_3 amount of 10 at.%. This suggests a stronger reduction of LiTFSI to LiF. Indeed, the relative intensity of the LiF peak increases from 2.5 V to 0.01 V for both TMG and TEG electrolytes, while only small changes are observed in atomic percentages. Compared to TEG, TMG displays higher LiF amounts at each investigated potential, indicating higher LiTFSI-salt decomposition with this electrolyte. No $C_2F_xLi_y$-like compounds are observed. S2p spectra in Fig. S6 of electrodes cycled in TMG and TEG display an intensive doublet at 169.3 eV which corresponds to the -SO_2 group in the LiTFSI-salt. The second doublet at 167 eV is ascribed to oxidized sulfur species such as -SO_x. Some works also assigned this species to Li_2SO_3 components [53]. During formation no additional sulfur decomposition products such as Li_2S, $Li_2S_2O_4$, Li_2SO_3 or Li_2SO are detected. N1s spectra in Fig. S5 display a peak at 399.8 eV corresponding to N-SO_2 groups. At 0.01 V, cells cycled TEG show an additional peak at 397.5 eV corresponding to Li_3N. With TMG, no such component is observed.

Cells cycled in the L-E/D reference electrolyte display two peaks corresponding to -CF_3 (689 eV) and LiF (685.1 eV) in Fig. 8. At 0.01 V, an additional peak emerges, which can be ascribed to groups in $C_2F_xLi_y$-like compounds [53]. Compared to the -CF_3 peak at 689.1 eV, these -CF_x components emerge at much lower binding energies of 687 eV. We explain this by the absence of neighboring -NSO_2 groups. Interestingly,

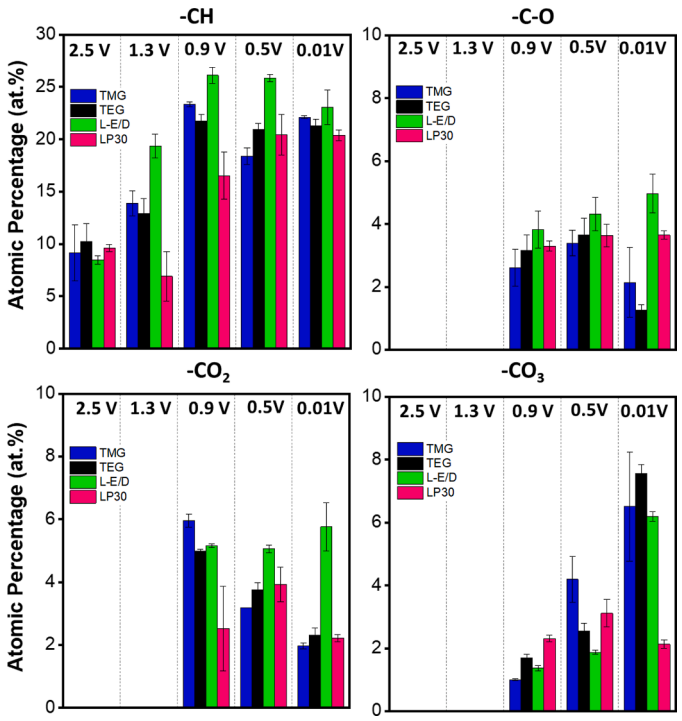

Fig. 7. Atomic percentages of detected SEI species -CH, -C-O, -CO_2, and -CO_3 of electrodes cycled in TMG, TEG, L-E/D, and LP30 electrolyte at 2.5 V, 1.3 V, 0. 9 V, 0.5 V, and 0.01 V. The error bars indicate the standard deviation between two measurements on one electrode.

both glyoxal-based electrolytes do not display this species. Similar to TMG and TEG, L-E/D shows an increase in the relative intensity of LiF from 2.5 V to 0.01 V. Also, S2p spectra exhibit two doublets at 169.5 eV and 166 eV, corresponding to -SO_2 groups and -SO_x or Li_2SO_3, respectively. Contrary to TMG and TEG, no increase is observed for the -SO_x or Li_2SO_3 species. N1s spectra show a peak at 399.9 eV ascribed to N-SO_2 groups. Like TEG, Li_3N emerges in the fully lithiated state at 0.01 V.

Cells cycled in the LP30 reference electrolyte show two peaks in Fig. 8 corresponding to LiF (685.1 eV) and a mixture of Li_xPF_y/Li_xPOF_y (687.2 eV). Both result from the decomposition of the electrolyte salt $LiPF_6$ [54–56]. Interestingly, LiF is already detected at 2.5 V, indicating $LiPF_6$ to be decomposing at higher potentials, most probable via hydrolysis [54,57]. An increase in LiF abundance can be observed from 2.5 V to 1.3 V, see Fig. 9. From 1.3 V to 0.5 V the detected amount of LiF decreases, while more Li_xPF_y/Li_xPOF_y is observed. Such a decrease might be due to the starting EC and DMC reduction, as is seen in the C1s spectra. In the fully lithiated state, LiF again increases in intensity, which can occur by the low potential and a more reactive SEI. P2p spectra of Fig. S6 display two doublets corresponding to Li_xPF_y (137 eV) and Li_xPOF_y (134.5 eV). Upon lithiation, the amount of detected Li_xPOF_y behaves similar to LiF, as it shows a decrease from 2.5 V to 0.5 V but a subsequent increase from 0.5 V to 0.01 V. Additionally, the LiF (F1s) and Li_xPOF_y (P2p) peak display a shift in binding energy of 0.3 eV at 0.01 V compared to 2.5 V-0.5 V. Because both species shift in parallel, we think this to be a combination of an electronic gradient and preferential charging effect for the salt species. Overall, all LiTFSI-containing electrolytes display lower atomic percentages of LiF, while $LiPF_6$-containing cells show 4-9 at.% more of this component.

Evolution of SEI composition during aging: To investigate SEI aging in the different electrolyte systems, XPS was conducted after 1, 10, and 100 cycles on electrodes in the delithiated state (i.e., at 1.5 V). Fig. 10 shows the C 1s spectra of electrodes cycled in TMG, TEG, L-E/D, and LP30 electrolyte, respectively. Derived atomic percentages from these data are summarized in Fig. 11. F1s spectra are displayed in Fig. 12 with corresponding atomic percentages in Fig. 13. Spectra of the remaining elements O1s, N1s, P2p, and S2p can be found in the supplementary information Fig. S7-9. An overview of all detected species can be found in Tables S2-5.

Solvent decomposition. The following species are found at the electrode surface for all four electrolytes, see Fig. 10: hydrocarbons (285 eV), -C-O groups (286.5 eV), -CO_2 groups (288.9 eV), and -CO_3 groups (290.4 eV). Electrodes cycled in TMG, TEG, and L-E/D show an additional peak at 293.2 eV corresponding to -CF_3 groups resulting from the remaining LiTFSI salt as previously discussed in the formation analysis part of this manuscript. Upon cycling, TMG and TEG display very similar trends in atomic percentages. While -C-O components remain at around 4 at.% throughout all 100 cycles, hydrocarbons, -CO_2, and -CO_3 groups increase in abundance. This suggests TMG and TEG solvents to be decomposing to -CH, -CO_2 and -CO_3 containing products upon prolonged cycling. After 100 cycles, a higher abundance in -CO_3 species is observed for TMG than for TEG. Similarly, -CO_3 components are increasing when cycling in L-E/D. However, -C-O components also increase, while a decrease is observed for -CO_2. For L-E/D, a much stronger increase in -C-O and -CO_3 species is observed. Cells cycled in LP30 exhibit an increase in hydrocarbons and -CO_2 compounds upon cycling. The amount of detected -C-O and -CO_3 however stays very similar between the 1st and the 100th cycle. However, the SEI formed by LP30 exhibits the highest abundance in -CO_3 out of all electrolytes.

In a similar way to the observation made for SEI formation, the composition of the organic part of SEI is affected by the electrolyte solvent during aging. SEIs formed in glyoxal-based electrolytes TMG and TEG display very similar compositions that are more abundant in hydrocarbons. By contrast, both SEI layers derived from carbonate-based electrolytes show higher contents of -C-O and -CO_3 species, which is expected for carbonate-based electrolytes [42].

Salt decomposition. The decomposition products of the different electrolyte salts LiTFSI and $LiPF_6$ can be followed in the F1s spectra displayed in Fig. 12. As seen during the SEI formation, two peaks are detected when cycling in TMG or TEG, namely LiF and -CF_3. While -CF_3 decreases upon cycling, the amount of detected LiF increases for both electrolytes from the 1st to the 10th cycle (i.e., 18 at.% for TMG and 10 at.% for TMG, see Fig. 13). After 100 cycles, LiF decreases by 14 at.% for TMG and 9 at.% for TEG. In all cases, TMG displays higher LiF abundance than TEG, indicating higher salt decomposition for the TMG electrolyte. In addition to fluorine-containing decomposition species, TMG and TEG show emerging Li_3N (397.4 eV), -SO_x or Li_2SO_3 (167.3 eV), and additional sulfur decomposition products (~163.9 eV and 161.8 eV), see Figs. S8 and S9. These additional sulfur decomposition products are already present after the 1st cycle with TMG, while they only emerge after 100 cycles with TEG. This observation might be explained by TEG forming a more stable SEI and suppressing LiTFSI salt decomposing to a stronger extent.

The F1s spectra of cells cycled in the L-E/D reference electrolyte display three peaks as already seen after 0.01 V, corresponding to -CF_3, $C_2F_xLi_y$, and LiF species. Upon cycling, the amount of detected LiF increases by 11 at.% from the 1st to the 10th cycle. Unlike TMG and TEG, the amount of LiF does not drop upon continued cycling but stays at around 12 at.%. The detected amount of -CF_3 compounds increases slightly upon cycling by 4 at.% from the 1st to the 100th cycle. Detected $C_2F_xLi_y$ species are decreasing upon cycling. Concerning N- and S-containing decomposition products, no Li_3N, nor -SO_x/Li_2SO_3 components are detected with L-E/D upon cycling.

The SEI formed by LP30 demonstrates an increase of both fluorine-containing species upon cycling (i.e., Li_xPF_y/Li_xPOF_y) while the amount of LiF decreases. Intensities of detected Li_xPOF_y species in P2p spectra of Fig. S9 remain similar throughout cycling.

Compared to the C1s spectra, where an increase in solvent decomposition is observed, no dramatic increase in salt decomposition is detected here. While the amount of measured LiF even decreases for TMG, TEG, and LP30, no changes are seen for L-E/D. As only the first 5-

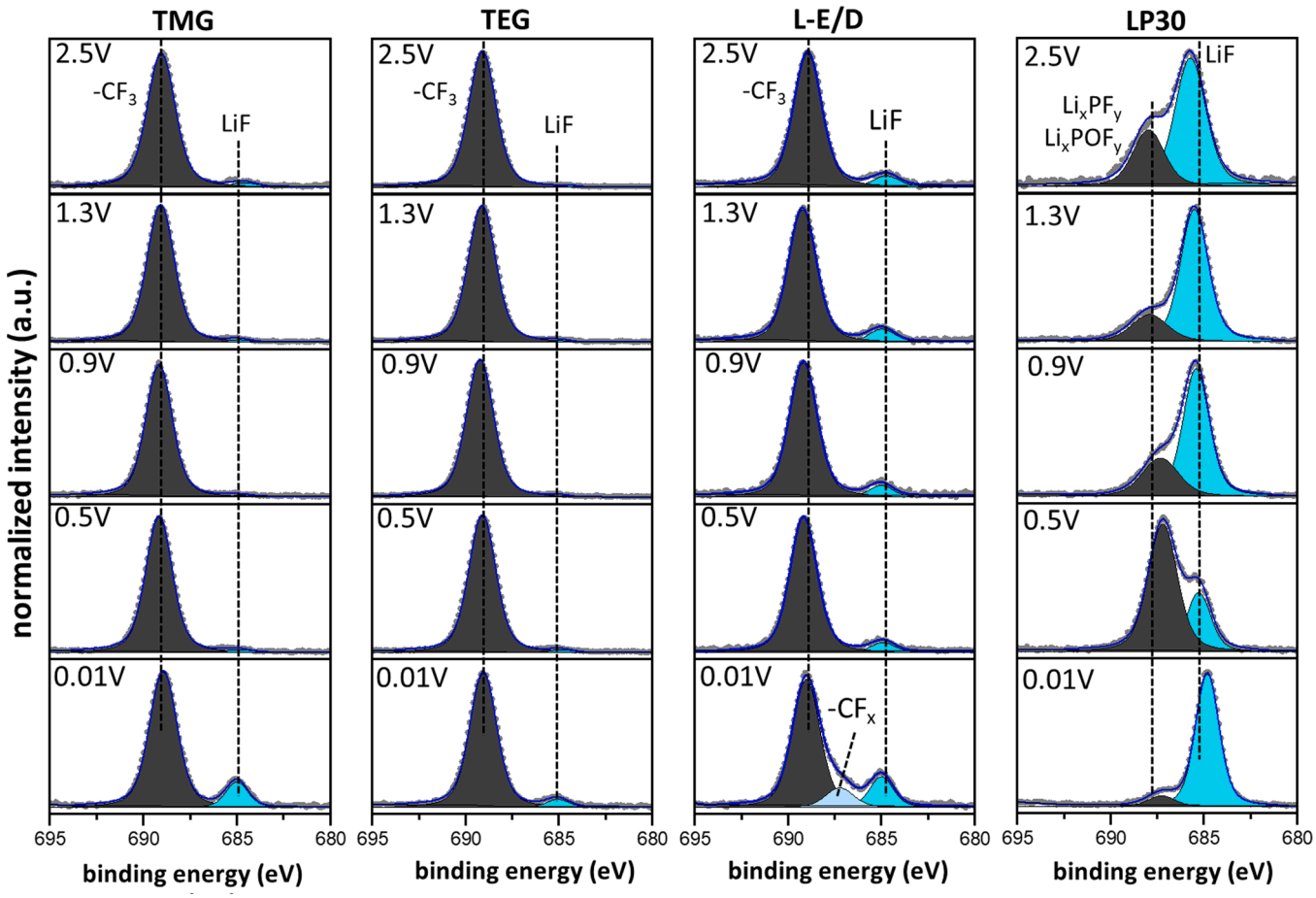

Fig. 8. F 1s photoelectron spectra of electrodes cycled in TMG, TEG, L-E/D, and LP30 electrolyte at 2.5 V, 1.3 V, 0. 9 V, 0.5 V, and 0.01 V.

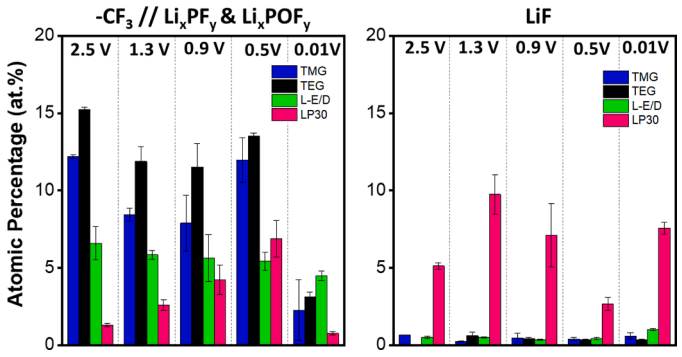

Fig. 9. Atomic percentages of LiF and-CF_3/-CF_x for electrodes cycled in TMG, TEG, and L-E/D at 2.5 V, 1.3 V, 0. 9 V, 0.5 V, and 0.01 V. For cells cycled in LP30, LiF and Li_xPF_y are displayed, also at 2.5 V, 1.3 V, 0. 9 V, 0.5 V, and 0.01 V. The error bars indicate the standard deviation between two measurements on one electrode.

10 nm of the SEI can be probed with the here used laboratory x-ray aluminum source, differences in composition of deeper layers cannot be identified. Nevertheless, the here observed increase of organic species in the outer SEI layer is known in the literature. It has been repeatedly observed for the outer SEI layer to consist of more organic layer, whereas the inner layer is more inorganic in nature [42,58].

SEI and electrode morphology. SEM images of a pristine Si/Gr electrode and electrode surfaces after 100 cycles are presented in Fig. 14. The uncycled electrode of Fig. 14(a) displays graphite as large rectangular-shaped particles, silicon as small and round shapes spread into different agglomerations, and carbon nanofibers as long tubes. After 100 cycles, all surfaces display pronounced changes in electrode morphology. In the case of TMG, L-E/D, and LP30 graphite particles are covered with electrolyte decomposition products. The previously sharp graphite edges are covered by bright and small particles, that are either closely sticking together or forming intricate networks. Corresponding magnifications show a strong SEI coverage of graphite, carbon nanofibers and silicon particles. However, it is difficult to differentiate between silicon particles and electrolyte decomposition products such as LiF. For all three cases, the surface morphology is very rough, suggesting continuous breaking and reformation of the SEI layer.

By contrast, the surface of the electrode cycled in TEG is covered by a smooth SEI film, which makes it difficult to distinguish between separate graphite particles. This difference in electrode surface morphology is also observed in the magnification, suggesting an extensive coverage of the electrode material. Furthermore, the SEI film does not exhibit obvious cracks, suggesting that TEG forms an SEI with an increased ability to accommodate to the volume changes of the Si/Gr electrode.

Correlating film-forming properties to electrochemical performance. In this study, we kept all experimental parameters the same except for the electrolytes. Therefore, the differences in cycling stability and SEI properties between Si/Gr electrodes can be related to the electrolyte formulations. The reference carbonate-based electrolytes showed similar capacity profiles with a pronounced capacity decrease after 20 cycles. Also, very similar retentions could be achieved after 100 cycles, indicating a loss in both silicon and graphite electrochemical activity. As can be expected of an SEI formed by the same carbonate-solvents (i.e., EC and DMC), the organic part of the SEI is very similar. The same species are detected, namely -CH, -C-O, -CO_2, and -CO_3. Furthermore, LiF is the main electrolyte salt decomposition product for both

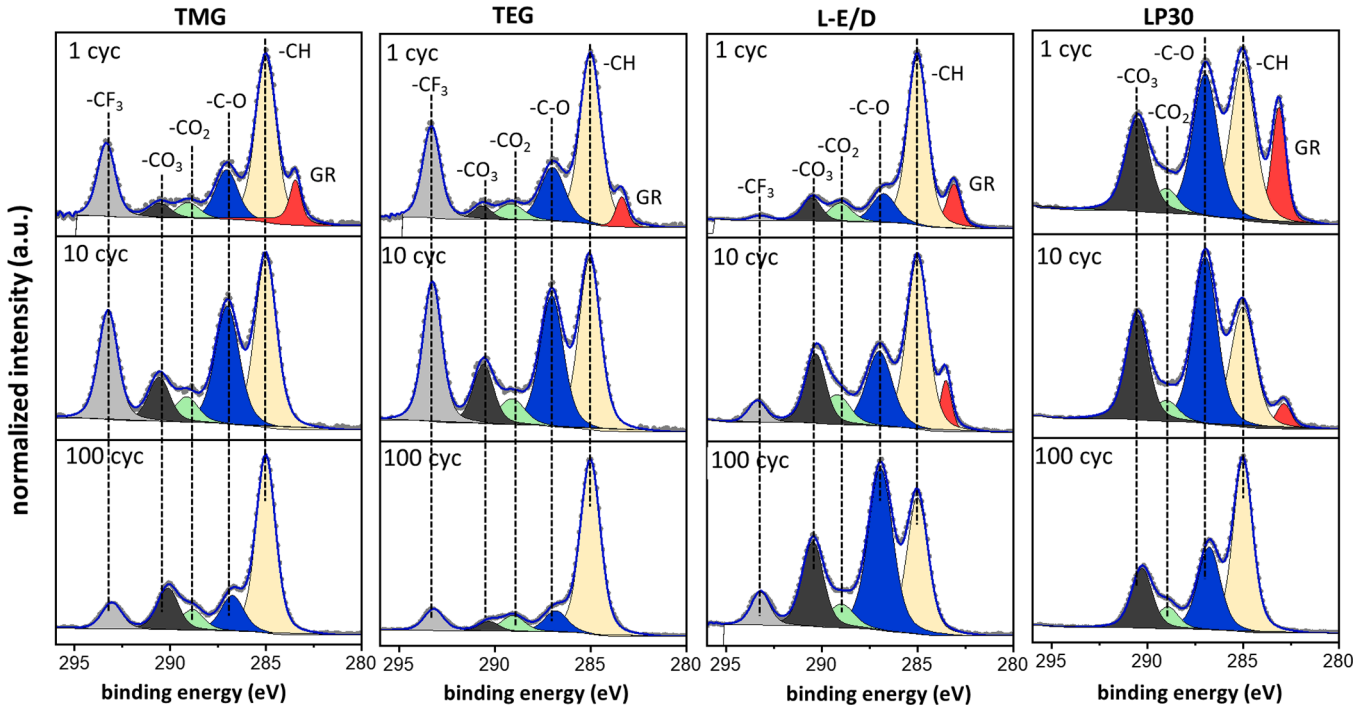

Fig. 10. C1s spectra of Si/Gr electrodes cycled in TMG, TEG, L-E/D, and LP30 electrolyte at C/10. Photoelectron spectra were taken after the following cycles: 1, 10, and 100 cycles.

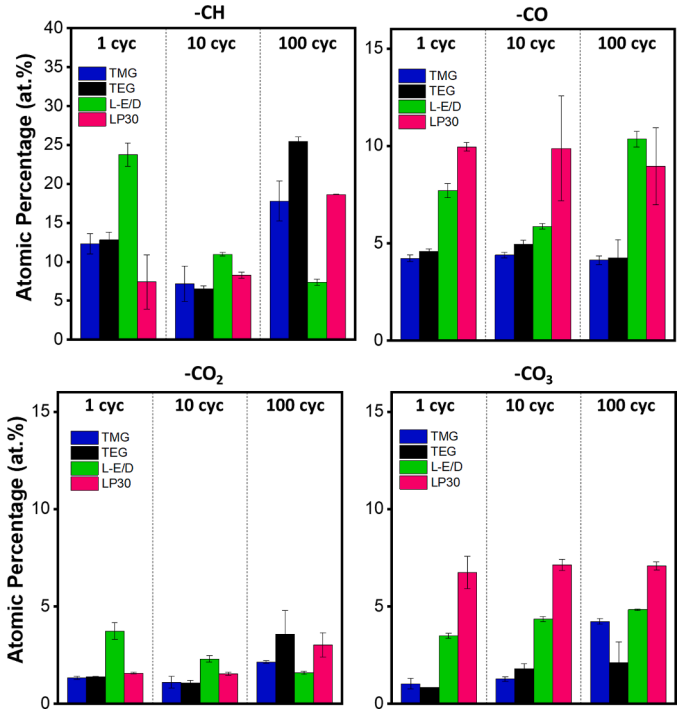

Fig. 11. Atomic percentages of different carbon-containing species in the SEI of Si/Gr electrodes cycled in TMG, TEG, L-E/D, and LP30 electrolyte at C/10. Photoelectron spectra were taken after the following cycles: 1, 10, and 100 cycles. The error bars indicate the standard deviation between two measurements on one electrode.

electrolytes. The observed changes in the abundance of the SEI species are not always identical, however, the following trend is observed: Upon cycling, the amount of detected LiF decreases, while an increase is seen for -C-O, and -CO_3 containing species. Also, changes in SEI thickness are comparable. After 10 cycles, the electrode material is still observed in the delithiated state. This suggests L-E/D and LP30 to be forming an SEI that is less stable upon the electrode volume changes as it breaks apart and reveals new electrode material. SEM pictures of electrode surfaces after 100 cycles show a very rough SEI film, indicating high mechanical strain as well as pulverization of the electrode material.

The investigated glyoxal-based electrolytes TMG and TEG only differ by a methyl group in the solvent molecule. Still, very different cycling profiles are observed. Cells cycled in TMG exhibit worse electrochemical performance than TEG and the two carbonate-bases electrolytes. A dramatic decrease of both silicon and graphite activity is already observed in the first 10 cycles. By contrast, TEG outperforms TMG, L-E/D, and LP30. While small losses are observed in silicon activity, graphite can completely retain its electrochemical activity. While small losses are observed in silicon activity, graphite can completely retain its electrochemical activity. Contrary to their obvious differences in electrochemical performance, TEG and TMG display similar trends in SEI composition and initial thickness, as seen with XPS. The SEI thickness evolution during long term cycling cannot be accurately estimated with XPS for these systems as in both cases, no bulk signal can be observed after the first cycle anymore, indicating an SEI thickness larger than the XPS probing depth. Concerning the SEI composition, the same functional groups are observed within the probed volume, namely -CH, -C-O, -CO_2, -CO_3, LiF, and -SO_x/ Li_2SO_3. Throughout the first formation cycle, the abundance of these compounds changes in a very similar way, suggesting the generation of comparable initial SEI films. While the amount of detected -CH, -C-O, and -CO_2 remains very similar for TEG and TMG, the following differences are observed when cycling in TMG-based electrolyte: 1) earlier LiTFSI salt decomposition, as seen in additional sulfur decomposition products from the 1st cycle on. These are not observed for the SEI formed by the TEG electrolyte, 2) higher LiF amounts are detected after 10 and 100 cycles, and 3) more carbonate species are detected after 100 cycles. The earlier and stronger salt decomposition with TMG as electrolyte solvent may indicate poor SEI stability. It should also be noted that the XPS probing depth is limited and possible divergences in deeper SEI layers cannot be detected. To analyze deeper layers, experiments such as sputtering or synchrotron

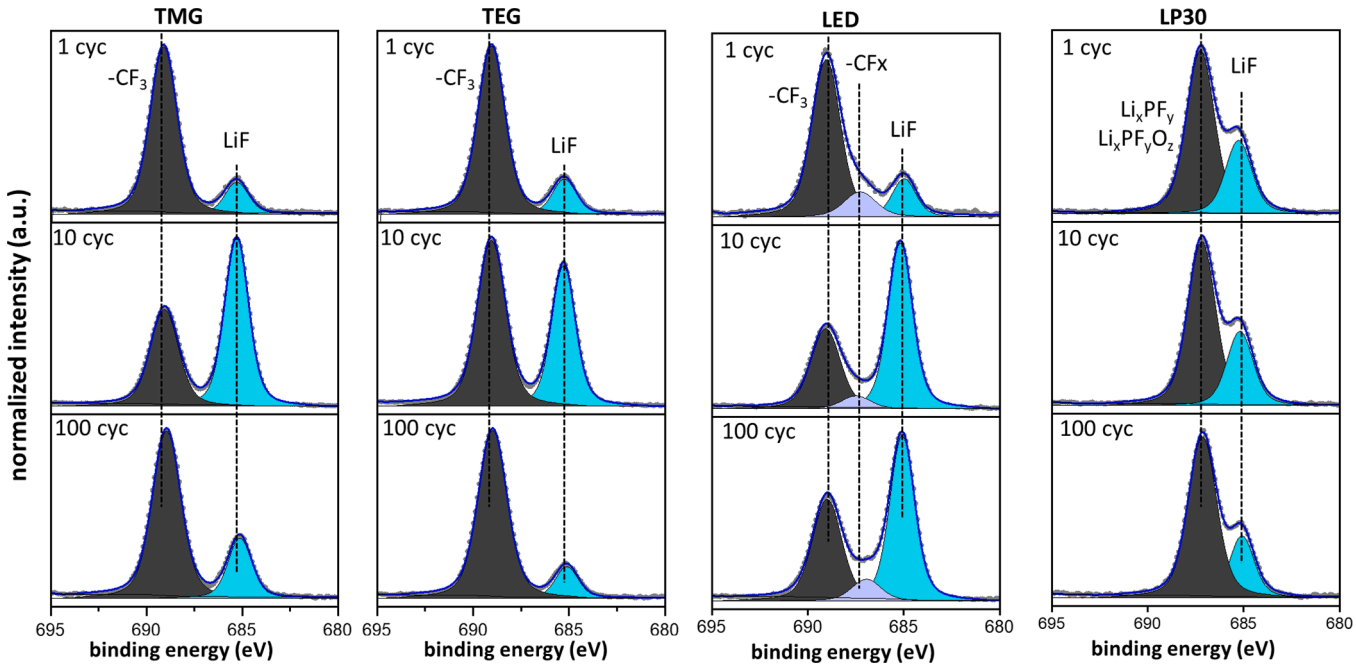

Fig. 12. F1s spectra of Si/Gr electrodes cycled in TMG, TEG, L-E/D, and LP30 electrolyte at C/10. Photoelectron spectra were taken after the following cycles: 1, 10, and 100 cycles.

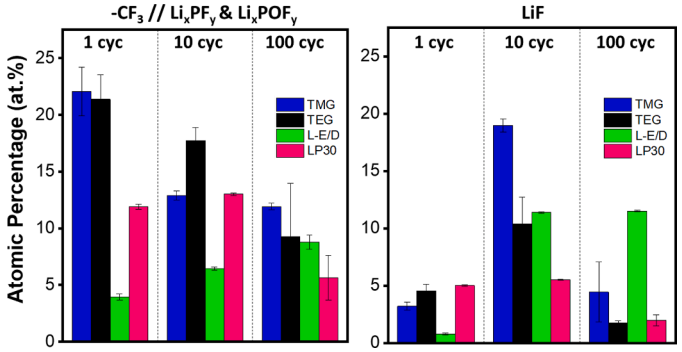

Fig. 13. F1s spectra of Si/Gr electrodes cycled in TMG, TEG, L-E/D, and LP30 electrolyte at C/10. Photoelectron spectra were taken after the following cycles: 1, 10, and 100 cycles. The error bars indicate the standard deviation between two measurements on one electrode.

measurements can be conducted, which are beyond the scope of this work. While XPS showed a more similar trend in SEI composition and initial thickness for TMG and TEG, SEM displays evident differences in the SEI morphology. With TMG a more fractured and rough surface morphology is observed, indicating repeated breaking of the SEI layer upon cycling. This further indicates a poor film forming ability of TMG on the Si/Gr anode. By contrast, TEG forms an SEI layer with a very interconnected coverage, suggesting a higher ability to adjust to the volume changes of the Si/Gr electrode. Alongside SEI formation on the Si/Gr anode, it is important to scrutinize the film-forming abilities of TEG and TMG on the lithium metal counter electrode. We observe that TMG shows higher reactivity against the lithium metal counter electrode than TEG. Fig. S10(1a) of the supporting information shows that after 100 cycles in TMG, the lithium counter electrode is completely black, very brittle, and contains almost no metallic lithium. This most likely results from poor lithium metal passivation by the TMG solvent. By contrast, the lithium electrode cycled in TEG, still displays a high amount of metallic and thereby electrochemically active lithium. The bigger size of the ethoxy groups in TEG could reduce reactions between the electrode and electrolyte due to steric hindrance. Such steric effects have been observed with other methoxy and ethoxy containing solvents [59,60].

In summary, TMG shows poor film-forming abilities on both lithium-metal electrodes and Si/Gr electrodes, explaining its poor electrochemical performance. When using TEG, a more stable interphase is formed on both electrodes. Our results further indicate that the good electrochemical performance of Si/Gr electrodes in TEG electrolytes might be related to the formation of an SEI that accommodates the silicon volume changes more easily.

4. Conclusion

In this work, we investigated the first use of glyoxal-based electrolytes (i.e., 1 M LiTFSI in TMG and 1 M LiTFSI in TEG) in combination with silicon-containing anodes. Two reference electrolytes LiTFSI-EC/DMC (L-E/D) and $LiPF_6$-EC/DMC (LP30) were analyzed in comparison. We showed that while the cell cycled in TMG performed worse than cells cycled in the reference electrolytes L-E/D and LP30, the cell cycled in TEG exhibited a much more stable capacity profile with overall higher capacities. The poor performance of TMG was related to a dramatic drop in both graphite and silicon activity after already 10 cycles. XPS did not supply a conclusive indication (in terms of SEI compositions and thicknesses) as to why TEG outperformed TMG so significantly, besides a more pronounced LiFTSI salt decomposition when using TMG as the solvent. Thus, future work will address the reactivity of TMG and TEG versus lithium metal and study glyoxal-based electrolytes in full cells. Analysis of the electrode morphology revealed TEG to form a smoother and continuously connected SEI. This surface layer most probably has higher ability to accommodate the silicon volume changes upon cycling, rendering TEG a very promising electrolyte candidate for realizing silicon-containing anodes with high capacity and high stability. Even without SEI stabilizing electrolyte additive or ionic conductivity enhancing co-solvent, TEG showed enhanced electrochemical performance with Si/Gr anodes compared to the standard LP30. Future studies will concentrate on further improving electrolytes based on TEG to become true alternatives to current commercial electrolytes with improved safety, environmental friendliness, and reduced toxicity.

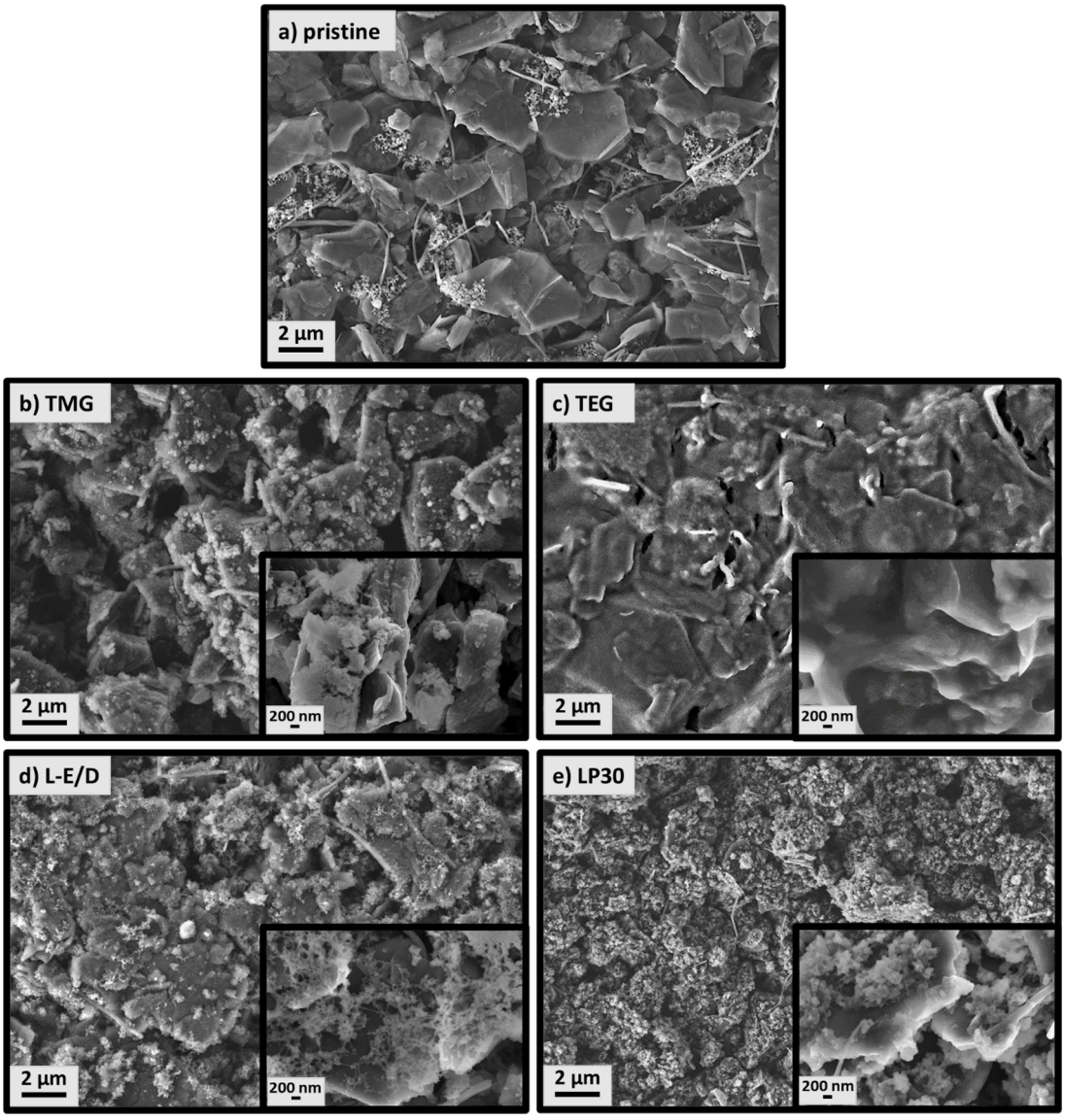

Fig. 14. SEM pictures of a pristine Si/Gr electrode (a) and after 100 cycles in TMG (b), TEG (c), L-E/D (d), and LP30 (e) electrolyte.

Author contribution statement for Manuscript Reference No. EA22-0675

L.G. and J.M oversaw the project; L.G. carried out the experiments and discussed the results with J.M., F.J. and A.B.; C.L. and A.B. provided the resources (TMG & TEG electrolytes); K.P. conducted SEM measurements, L.G. wrote the preliminary draft, all authors contributed to interpreting the results and reviews and revised the manuscript.

Declaration of Competing Interest

The authors declare that they have no known competing financial interests or personal relationships that could have appeared to influence the work reported in this paper.

Acknowledgment

The authors are grateful to the German Federal Ministry of Education and Research (FKZ 03XP0131) for financial support. Furthermore, the authors wish to thank the Friedrich Schiller University Jena and the Deutsche Forschungsgemeinschaft (DFG) within the project "The combined use of computational screening and electrochemical characterization for the identification of new electrolyte components for supercapacitors" for the financial support. This work contributes to the research performed at CELEST (Center for Electrochemical Energy Storage Ulm-Karlsruhe).

Supplementary materials

Supplementary material associated with this article can be found, in the online version, at doi:10.1016/j.electacta.2022.140642.

References

[1] M.N. Obrovac, L. Christensen, D.B. Le, J.R. Dahn, Alloy design for lithium-ion battery anodes, J. Electrochem. Soc. 154 (9) (2007) A849, https://doi.org/10.1149/1.2752985.
[2] T. Schott, R. Robert, S. Pacheco Benito, P.A. Ulmann, P. Lanz, S. Zürcher, M. E. Spahr, P. Novák, S. Trabesinger, Cycling behavior of silicon-containing graphite electrodes, part B: effect of the silicon source, J. Phys. Chem. C 121 (46) (2017) 25718–25728, https://doi.org/10.1021/acs.jpcc.7b08457.
[3] F. Jeschull, Y. Surace, S. Zürcher, M.E. Spahr, P. Novák, S. Trabesinger, Electrochemistry and morphology of graphite negative electrodes containing silicon as capacity-enhancing electrode additive, Electrochim. Acta 320 (2019) 1–12, https://doi.org/10.1016/j.electacta.2019.134602.
[4] M. Marinaro, D. Yoon, hwan, G. Gabrielli, P. Stegmaier, E. Figgemeier, P.C. Spurk, D. Nelis, G. Schmidt, J. Chauveau, P. Axmann, M. Wohlfahrt-Mehrens, High

Performance 1.2 Ah Si-alloy/graphite|lini0.5Mn0.3co0.2o2 prototype Li-ion battery, J. Power Sources 357 (2017) 188–197, https://doi.org/10.1016/j.jpowsour.2017.05.010.
[5] T. Zhang, H. Yue, H. Qiu, Y. Wei, C. Wang, G. Chen, D. Zhang, Nano-particle assembled porous core-shell ZnMn 2 O 4 microspheres with superb performance for lithium batteries, Nanotechnology 28 (10) (2017), 105403, https://doi.org/10.1088/1361-6528/aa5a49.
[6] M. Klett, J.A. Gilbert, K.Z. Pupek, S.E. Trask, D.P. Abraham, Layered oxide, graphite and silicon-graphite electrodes for lithium-ion cells: effect of electrolyte composition and cycling windows, J. Electrochem. Soc. 164 (1) (2017) A6095–A6102, https://doi.org/10.1149/2.0131701jes.
[7] V.L. Chevrier, L. Liu, D.B. Le, J. Lund, B. Molla, K. Reimer, L.J. Krause, L.D. Jensen, E. Figgemeier, K.W. Eberman, Evaluating Si-based materials for Li-ion batteries in commercially relevant negative electrodes, J. Electrochem. Soc. 161 (5) (2014) A783–A791, https://doi.org/10.1149/2.066405jes.
[8] G.G. Eshetu, H. Zhang, X. Judez, H. Adenusi, M. Armand, S. Passerini, E. Figgemeier, Production of high-energy Li-ion batteries comprising silicon-containing anodes and insertion-type cathodes, Nat. Commun. 12 (1) (2021) 1–14, https://doi.org/10.1038/s41467-021-25334-8.
[9] D.S.M. Iaboni, M.N. Obrovac, Li 15 Si 4 formation in silicon thin film negative electrodes, J. Electrochem. Soc. 163 (2) (2016) A255–A261, https://doi.org/10.1149/2.0551602jes.
[10] M.N. Obrovac, V.L. Chevrier, Alloy negative electrodes for Li-ion batteries, Chem. Rev. 114 (23) (2014) 11444–11502, https://doi.org/10.1021/cr500207g.
[11] M. Wetjen, D. Pritzl, R. Jung, S. Solchenbach, R. Ghadimi, H.A. Gasteiger, Differentiating the degradation phenomena in silicon-graphite electrodes for lithium-ion batteries, J. Electrochem. Soc. 164 (12) (2017) A2840–A2852, https://doi.org/10.1149/2.1921712jes.
[12] S. Chae, S.H. Choi, N. Kim, J. Sung, J. Cho, Integration of graphite and silicon anodes for the commercialization of high-energy lithium-ion batteries, Angew. Chemie - Int. Ed. 59 (1) (2020) 110–135, https://doi.org/10.1002/anie.201902085.
[13] R. Petibon, V.L. Chevrier, C.P. Aiken, D.S. Hall, S.R. Hyatt, R. Shunmugasundaram, J.R. Dahn, Studies of the capacity fade mechanisms of LiCoO 2 /Si-alloy: graphite cells, J. Electrochem. Soc. 163 (7) (2016) A1146–A1156, https://doi.org/10.1149/2.0191607jes.
[14] M. Wetjen, M. Trunk, L. Werner, R. Gernhäuser, B. Märkisch, Z. Révay, R. Gilles, H. A. Gasteiger, Quantifying the distribution of electrolyte decomposition products in silicon-graphite electrodes by neutron depth profiling, J. Electrochem. Soc. 165 (10) (2018) A2340–A2348, https://doi.org/10.1149/2.1341810jes.
[15] B. Philippe, R. Dedryvère, J. Allouche, F. Lindgren, M. Gorgoi, H. Rensmo, D. Gonbeau, K. Edström, Nanosilicon electrodes for lithium-ion batteries: interfacial mechanisms studied by hard and soft x-ray photoelectron spectroscopy, Chem. Mater. 24 (6) (2012) 1107–1115, https://doi.org/10.1021/cm2034195.
[16] Y. Jin, N.J.H. Kneusels, P.C.M.M. Magusin, G. Kim, E. Castillo-Martínez, L. E. Marbella, R.N. Kerber, D.J. Howe, S. Paul, T. Liu, C.P. Grey, Identifying the structural basis for the increased stability of the solid electrolyte interphase formed on silicon with the additive fluoroethylene carbonate, J. Am. Chem. Soc. 139 (42) (2017) 14992–15004, https://doi.org/10.1021/jacs.7b06834.
[17] J.B. Goodenough, Y. Kim, Challenges for rechargeable Li batteries †, Chem. Mater. 22 (3) (2010) 587–603, https://doi.org/10.1021/cm901452z.
[18] Eds M, R.J. Yoshio, A.K. Brodd, Lithium-Ion Batteries: Science and Technologies, Springer, New York, 2010.
[19] Eds C. Daniel, J.O. B, Handbook of Battery Materials, 2nd Editio, Wiley-VCH: Weinheim, 2011.
[20] S.F. Lux, J. Chevalier, I.T. Lucas, R. Kostecki, HF formation in LiPF6-based organic carbonate electrolytes, ECS Electrochem. Lett. 2 (12) (2013) A121–A123, https://doi.org/10.1149/2.005312eel.
[21] D. Doughty, E.P. Roth, A general discussion of Li ion battery safety, Electrochem. Soc. Interface 21 (2) (2012) 37–44, https://doi.org/10.1149/2.F03122if.
[22] E. Markevich, G. Salitra, D. Aurbach, Fluoroethylene carbonate as an important component for the formation of an effective solid electrolyte interphase on anodes and cathodes for advanced Li-ion batteries, ACS Energy Lett. 2 (6) (2017) 1337–1345, https://doi.org/10.1021/acsenergylett.7b00163.
[23] E. Markevich, K. Fridman, R. Sharabi, R. Elazari, G. Salitra, H.E. Gottlieb, G. Gershinsky, A. Garsuch, G. Semrau, M.A. Schmidt, D. Aurbach, Amorphous columnar silicon anodes for advanced high voltage lithium ion full cells: dominant factors governing cycling performance, J. Electrochem. Soc. 160 (10) (2013) A1824–A1833, https://doi.org/10.1149/2.085310jes.
[24] T. Jaumann, J. Balach, U. Langklotz, V. Sauchuk, M. Fritsch, A. Michaelis, V. Teltevskij, D. Mikhailova, S. Oswald, M. Klose, G. Stephani, R. Hauser, J. Eckert, L. Giebeler, Lifetime vs. rate capability: understanding the role of FEC and VC in high-energy Li-ion batteries with nano-silicon anodes, Energy Storage Mater. 6 (2017) 26–35, https://doi.org/10.1016/j.ensm.2016.08.002.
[25] V. Etacheri, O. Haik, Y. Goffer, G.A. Roberts, I.C. Stefan, R. Fasching, D. Aurbach, Effect of fluoroethylene carbonate (FEC) on the performance and surface chemistry of Si-nanowire Li-ion battery anodes, Langmuir 28 (1) (2012) 965–976, https://doi.org/10.1021/la203712s.
[26] R. Jung, M. Metzger, D. Haering, S. Solchenbach, C. Marino, N. Tsiouvaras, C. Stinner, H.A. Gasteiger, Consumption of fluoroethylene carbonate (FEC) on Si-C composite electrodes for Li-ion batteries, J. Electrochem. Soc. 163 (8) (2016) A1705–A1716, https://doi.org/10.1149/2.0951608jes.
[27] L.H. Hess, S. Wankmüller, L. Köps, A. Bothe, A. Balducci, Stable acetals of glyoxal as electrolyte solvents for lithium-ion batteries, Batter. Supercaps 2 (10) (2019) 852–857, https://doi.org/10.1002/batt.201900051.
[28] L. Köps, C. Leibing, L.H. Hess, A. Balducci, Mixtures of glyoxylic acetals and organic carbonates as electrolytes for lithium-ion batteries, J. Electrochem. Soc. 168 (1) (2021), 010513, https://doi.org/10.1149/1945-7111/abd604.
[29] J. Atik, S. Röser, R. Wagner, D. Berghus, M. Winter, I. Cekic-Laskovic, Acyclic acetals in propylene carbonate-based electrolytes for advanced and safer graphite-based lithium ion batteries, J. Electrochem. Soc. 167 (4) (2020), 040509, https://doi.org/10.1149/1945-7111/ab72dc.
[30] L.H. Heß, A. Balducci, Glyoxal-based solvents for electrochemical energy-storage devices, ChemSusChem 11 (12) (2018) 1919–1926, https://doi.org/10.1002/cssc.201800375.
[31] C. Leibing, A. Balducci, Glyoxylic-acetal-based electrolytes in combination with soft and hard carbon electrodes for lithium-ion batteries: an evaluation of room and high temperature performance, J. Electrochem. Soc. 168 (9) (2021), 090533, https://doi.org/10.1149/1945-7111/ac23a2.
[32] K.L. Parry, A.G. Shard, R.D. Short, R.G. White, J.D. Whittle, A. Wright, ARXPS characterisation of plasma polymerised surface chemical gradients, Surf. Interface Anal. 38 (2006) 1497–1504, https://doi.org/10.1002/sia.2400.
[33] C. Didier, W.K. Pang, Z. Guo, S. Schmid, V.K. Peterson, Phase evolution and intermittent disorder in electrochemically lithiated graphite determined using in operando neutron diffraction, Chem. Mater. 32 (6) (2020) 2518–2531, https://doi.org/10.1021/acs.chemmater.9b05145.
[34] C. Sole, N.E. Drewett, L.J. Hardwick, Insitu Raman study of lithium-ion intercalation into microcrystalline graphite, Faraday Discuss. 172 (2014) 223–237, https://doi.org/10.1039/c4fd00079j.
[35] C.J. Wen, R.A. Huggins, Chemical diffusion in intermediate phases in the lithium-silicon system, J. Solid State Chem. 37 (3) (1981) 271–278, https://doi.org/10.1016/0022-4596(81)90487-4.
[36] P. Limthongkul, Y.Il Jang, N.J. Dudney, Y.M Chiang, Electrochemically-driven solid-state amorphization in lithium-silicon alloys and implications for lithium storage, Acta Mater. 51 (4) (2003) 1103–1113, https://doi.org/10.1016/S1359-6454(02)00514-1.
[37] M.J. Chon, V.A. Sethuraman, A. McCormick, V. Srinivasan, P.R. Guduru, Real-time measurement of stress and damage evolution during initial lithiation of crystalline silicon, Phys. Rev. Lett. 107 (4) (2011) 1–4, https://doi.org/10.1103/PhysRevLett.107.045503.
[38] B. Key, M. Morcrette, J.M. Tarascon, C.P. Grey, Pair distribution function analysis and solid state NMR studies of silicon electrodes for lithium ion batteries: understanding the (de)lithiation mechanisms, J. Am. Chem. Soc. 133 (3) (2011) 503–512, https://doi.org/10.1021/ja108085d.
[39] J. Li, J.R. Dahn, An in situ X-ray diffraction study of the reaction of Li with crystalline Si, J. Electrochem. Soc. 154 (3) (2007) A156, https://doi.org/10.1149/1.2409862.
[40] T.D. Hatchard, J.R. Dahn, In situ XRD and electrochemical study of the reaction of lithium with amorphous silicon, J. Electrochem. Soc. 151 (6) (2004) A838, https://doi.org/10.1149/1.1739217.
[41] A. Netz, R.A. Huggins, Amorphous silicon formed in situ as negative electrode reactant in lithium cells, Solid State Ionics 175 (1-4) (2004) 215–219, https://doi.org/10.1016/j.ssi.2003.11.048.
[42] S.K. Heiskanen, J. Kim, B.L. Lucht, Generation and evolution of the solid electrolyte interphase of lithium-ion batteries, Joule 3 (10) (2019) 2322–2333, https://doi.org/10.1016/j.joule.2019.08.018.
[43] C. Cao, H.G. Steinrück, B. Shyam, M.F. Toney, The atomic scale electrochemical lithiation and delithiation process of silicon, Adv. Mater. Interfaces 4 (22) (2017) 1–7, https://doi.org/10.1002/admi.201700771.
[44] G.M. Veith, M. Doucet, J.K. Baldwin, R.L. Sacci, T.M. Fears, Y. Wang, J. F. Browning, Direct determination of solid-electrolyte interphase thickness and composition as a function of state of charge on a silicon anode, J. Phys. Chem. C 119 (35) (2015) 20339–20349, https://doi.org/10.1021/acs.jpcc.5b06817.
[45] T.M. Fears, M. Doucet, J.F. Browning, J.K.S. Baldwin, J.G. Winiarz, H. Kaiser, H. Taub, R.L. Sacci, G.M. Veith, Evaluating the solid electrolyte interphase formed on silicon electrodes: a comparison of: ex situ x-ray photoelectron spectroscopy and in situ neutron reflectometry, Phys. Chem. Chem. Phys. 18 (20) (2016) 13927–13940, https://doi.org/10.1039/c6cp00978f.
[46] D. Briggs, Surface Analysis of Polymers by XPS Ans Static SIMS, Cambridge University Press, 1998, https://doi.org/10.1017/CBO9780511525261.
[47] P. Verma, P. Maire, P. Novák, A review of the features and analyses of the solid electrolyte interphase in Li-ion batteries, Electrochim. Acta 55 (22) (2010) 6332–6341, https://doi.org/10.1016/j.electacta.2010.05.072.
[48] H. Ota, Y. Sakata, A. Inoue, S. Yamaguchi, Analysis of vinylene carbonate derived SEI layers on graphite anode, J. Electrochem. Soc. 151 (10) (2004) A1659, https://doi.org/10.1149/1.1785795.
[49] S.J. An, J. Li, C. Daniel, D. Mohanty, S. Nagpure, D.L. Wood, The state of understanding of the lithium-ion-battery graphite solid electrolyte interphase (SEI) and its relationship to formation cycling, Carbon NY 105 (2016) 52–76, https://doi.org/10.1016/j.carbon.2016.04.008.
[50] S. Leroy, H. Martinez, R. Dedryvère, D. Lemordant, D. Gonbeau, Influence of the lithium salt nature over the surface film formation on a graphite electrode in li-ion batteries: an XPS study, Appl. Surf. Sci. 253 (11) (2007) 4895–4905, https://doi.org/10.1016/j.apsusc.2006.10.071.
[51] B.S. Parimalam, B.L. Lucht, Reduction reactions of electrolyte salts for lithium ion batteries: LiPF 6, LiBF 4, LiDFOB, LiBOB, and LiTFSI, J. Electrochem. Soc. 165 (2) (2018) 251–255, https://doi.org/10.1149/2.0901802jes.
[52] D. Aurbach, I. Weissman, A. Schechter, H. Cohen, X-ray photoelectron spectroscopy studies of lithium surfaces prepared in several important electrolyte solutions. a comparison with previous studies by fourier transform infrared

spectroscopy, Langmuir 12 (16) (1996) 3991–4007, https://doi.org/10.1021/la9600762.
[53] C. Xu, B. Sun, T. Gustafsson, K. Edström, D. Brandell, M. Hahlin, Interface layer formation in solid polymer electrolyte lithium batteries: an XPS study, J. Mater. Chem. A 2 (20) (2014) 7256–7264, https://doi.org/10.1039/c4ta00214h.
[54] D. Aurbach, B. Markovsky, A. Shechter, Y. Ein-Eli, H. Cohen, A comparative study of synthetic graphite and li electrodes in electrolyte solutions based on ethylene carbonate-dimethyl carbonate mixtures, J. Electrochem. Soc. 143 (12) (1996) 3809–3820, https://doi.org/10.1149/1.1837300.
[55] T. Eriksson, A.M. Andersson, A.G. Bishop, C. Gejke, T. Gustafsson, J.O Thomas, Surface analysis of LiMn[Sub 2]O[Sub 4] electrodes in carbonate-based electrolytes, J. Electrochem. Soc. 149 (1) (2002) A69, https://doi.org/10.1149/1.1426398.
[56] D. Aurbach, Review of selected electrode-solution interactions which determine the performance of Li and Li Ion batteries, J. Power Sources 89 (2) (2000) 206–218, https://doi.org/10.1016/S0378-7753(00)00431-6.
[57] P.G. Kitz, P. Novák, E.J. Berg, Influence of water contamination on the SEI formation in Li-ion cells: an operando EQCM-D study, ACS Appl. Mater. Interfaces 12 (13) (2020) 15934–15942, https://doi.org/10.1021/acsami.0c01642.
[58] E. Peled, D. Bar Tow, A. Merson, A. Gladkich, L. Burstein, D. Golodnitsky, Composition, depth profiles and lateral distribution of materials in the SEI built on HOPG-TOF SIMS and XPS studies, J. Power Sources (2001), https://doi.org/10.1016/S0378-7753(01)00505-5.
[59] T.D. Pham, K.K. Lee, Simultaneous stabilization of the solid/cathode electrolyte interface in lithium metal batteries by a new weakly solvating electrolyte, Small 17 (20) (2021) 1–12, https://doi.org/10.1002/smll.202100133.
[60] Y. Chen, Z. Yu, P. Rudnicki, H. Gong, Z. Huang, S.C. Kim, J.C. Lai, X. Kong, J. Qin, Y. Cui, Z. Bao, Steric effect tuned ion solvation enabling stable cycling of high-voltage lithium metal battery, J. Am. Chem. Soc. 143 (44) (2021) 18703–18713, https://doi.org/10.1021/jacs.1c09006.